Transverse resolution improvement using rotating-grating time-multiplexing approach

Vicente Mico,[1] Ofer Limon,[2] Aviram Gur,[2] Zeev Zalevsky,[2,*] and Javier García[3]

[1]*AIDO, Technological Institute of Optics, Colour and Imaging, C/. Nicolás Copérnico, 7-13 Parc Tecnològic, 46980 Paterna (Valencia) Spain*
[2]*School of Engineering, Bar-Ilan University, Ramat-Gan, 52900 Israel*
[3]*Departamento de Óptica, Universitat de València, C/. Dr. Moliner, 50. 46100 Burjassot, Spain*
**Corresponding author: zalevsz@macs.biu.ac.il*

Received September 13, 2007; revised February 6, 2008; accepted February 10, 2008; posted March 10, 2008 (Doc. ID 87415); published April 23, 2008

The ability to improve the limited resolving power of optical imaging systems while approaching the theoretical diffraction limit has been an attractive discipline with growing interest over the last years due to its benefits in many applied optics systems. This paper presents a new approach to achieve transverse superresolution in far-field imaging systems, with direct application in both digital microscopy and digital holographic microscopy. Theoretical analysis and computer simulations show the validity of the presented approach.
© 2008 Optical Society of America
OCIS codes: 100.6640, 170.0110, 110.4850.

1. INTRODUCTION

Since Ernst Abbe [1] discovered at the end of the 19th century that the resolution of an optical imaging system is limited by diffraction, there have been a lot of attempts to go beyond this resolution limit. Abbe's work was applied to the field of microscopy, and it concludes that conventional high-resolution microscopy needs high numerical aperture (NA) objectives. However, high NA imaging lenses are costly and not always practical (depending on the application).

In accordance with Abbe's theory, filter theory applied to the spatial-frequency domain suggests that an optical imaging system acts as a low-bandpass filter selecting the low spatial frequencies of the object's spectrum [2]. Thus, the imaging system can be represented in the spatial-frequency domain by a limited aperture, which limits the maximum resolution that can be achieved with this imaging system. In summary, with a fixed illumination wavelength, the resolving power of an imaging system is defined as a function of its NA and can reach the $\lambda/2$ maximum value for air immersion optical systems and incoherent illumination. In that sense, the aim of superresolution (SR) techniques is to produce an improvement in the resolution limit without changes in the physical properties of the optical system in comparison with the spatial resolution presented by the same optical system in the absence of such approach. Based on this concept, many approaches have been proposed during the years to achieve SR in several disciplines such as near-field [3] and far-field [4] imaging, computational SR by digital algorithms [5], superresolving pupils using apodization techniques [6], and imaging by scanning procedures [7].

The present paper is devoted to far-field imaging SR techniques. These techniques can be understood as the generation of a synthetic aperture (SA) that expands the frequency coverage of the optical system beyond the limit defined by its cutoff frequency, that is, beyond its physical limited aperture. This procedure needs information theory [8–11] and *a priori* knowledge of the input object. By knowing that the object belongs to a certain class [12,13], it is possible to encode useful additional information regarding the object into unused channels of the optical system in such a way that it will pass through the system limited aperture. Some examples of such *a priori* information are that the object may be approximately time independent [14,15], or polarization independent [16], or wavelength independent [17], or one-dimensional (1-D) [18], or with limited intensity dynamic range [19]. In our case, we are interested in encoding spatial-frequency content of the object into the temporal degree of freedom by knowing that the object is temporally restricted. With the appropriate decoding process of such additional information, a superresolved image with enhanced spatial resolution can be obtained.

The manuscript is organized as follows. Section 2 provides a wide introduction to time-multiplexing SR. Section 3 presents a new approach to achieve transverse SR in both digital imaging and digital holographic imaging. Sections 4 and 5 include a theoretical analysis regarding our approach, while Sections 6 and 7 provide proof of concept as a simulation process. Finally, Section 8 concludes the paper.

2. TIME-MULTIPLEXING SUPERRESOLUTION

As previously shown, time multiplexing is a well-known SR approach applied to temporally restricted objects and can be implemented in a wide variety of ways [4,13–15]. The basic idea underlying a time-multiplexing SR approach is to downshift the high-frequency components of the object's spectrum to low frequency ones. This is ac-

complished by encoding the object spatial-frequency information into temporal-frequency information. Thus, those spatial-frequency components that are not transmitted by the system's aperture under conventional operation now fall inside and can pass through it. Obviously, this temporal-frequency coding needs to be decoded to obtain a high-resolution image; that is, the additional spatial-frequency information must be returned to its original position in the object's spectrum. Time-multiplexing SR has also been interpreted in the Wigner space by means of the space–bandwidth product adaptation [20,21].

Bearing in mind this working principle, many approaches use illumination through physical gratings to achieve the SR effect [13,15,18,22–24]. But many of them have the main drawback related to the need for attaching the encoding grating to the input plane [13,15,18]. One way to avoid such physical grating attachment is to pay with field of view instead of time [22–24]. Another way is by using optically generated gratings [25–30]. Thus, structured illumination microscopy [25], patterned excitation microscopy [26], laterally modulated excitation microscopy [27], and harmonic excitation light microscopy [28] have been proposed as methods to improve spatial resolution by means of SA generation in fluorescence microscopy. SR microscopy via structured illumination light and optical nonlinearity has also been applied to fluorescence microscopy [29,30].

Another way to achieve time-multiplexing SR is by using speckle patterns [31,32] instead of grating ones. Speckle patterns can be understood as a continuous case of the discrete one (represented by a diffraction grating) in which one can achieve two-dimensional (2-D) SR by simply coding–decoding the input and the output, respectively, with a given speckle pattern. Moreover, speckle pattern projection systems appear as simpler setups in comparison with the projection systems used in structured illumination.

Time-multiplexing SR can also be attained using coherence coding [33,34]. In this case, the mutual intensity function of the illumination beam is used to encode spatial information in a way analogous to time multiplexing but with multiplexing time slots that are given by the coherence time of the illumination beam. Coherence coding can also be obtained by using incoherent light interferometry and applying it to SR [35,36]. Because the time variation of most objects is lower than the coherence time of the source—that is, they can be considered temporally restricted in practice—the information coding can be implicitly made on the coherence of the illumination source. After that, interferometric image-plane recording with a postprocessing digital stage allows the needed decoding to achieve the SR effect.

Over the past years, time-multiplexing has been combined with digital holography [37–50] with the motivation of recovering both amplitude and phase distribution of the sample under test. Thus, optical coherent tomography and three-dimensional microscopy [37,38], interferometric lithography [39], polarization imaging [40], phase-aberration and image-distortion compensation [41,42], phase-shifting digital holography [43], and interferometric imaging [35,36,44–48] have been proposed as new methods with a real potential in industrial applications. In particular, a significant case of interferometric imaging is obtained in the field of microscopy [44–50], where SA generation permits high-resolution images using low-NA microscope lenses. These techniques are based on producing an off-axis illumination onto the object to downshift its high-frequency content and to enable its transmission through the system limited aperture in a similar way as gratings and speckle are able to accomplish. After that, and using holographic image plane recording, a SA is generated by digital filtering and a relocation of each transmitted frequency band to its original position in the object's spectrum. And finally, a superresolved image can be obtained by simple Fourier transformation (FT) of the information contained in the SA.

3. ROTATING-GRATING APPROACH

In this section, a new approach to achieve time-multiplexing, 2-D SR in imaging systems via a rotating grating and digital postprocessing is presented. Although the analysis included is deduced for a unity magnification imaging system in order to make the involved theory simpler, the approach is directly applicable to the field of microscopy.

In the suggested approach, a physical grating that is placed near the input object (but not in close contact) is used to generate structured illumination over the input object. Thus, provided that the diffracted beams of the grating overlap over the imaged region of the object, structured illumination is ensured, and the problems arising from the need to attach the grating physically to the object at the input plane are eliminated. Moreover, because the decoding process is performed digitally as in [15], the approach presented avoids the need for synchronization between both encoding–decoding gratings during the SR process.

The concept of the proposed method can be easily understood through the optical setup shown in Fig. 1. We call this setup *digital imaging approach* (DIA). For simplicity, to show the performance of the proposed approach, let us assume that the imaging system has a 4F configuration. Thus, the input object is imaged through two iden-

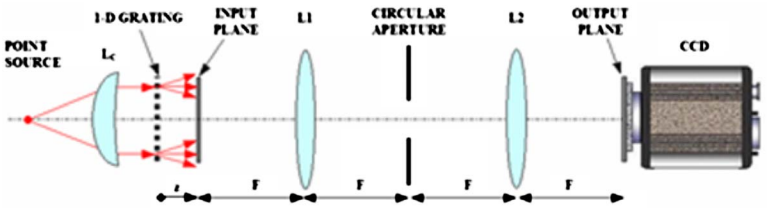


Fig. 1. (Color online) Optical setup for the DIA. The 1-D grating is mounted on a rotatable platform to accomplish the 2-D SR process.

tical lenses L1 and L2 onto a CCD camera that records the intensity distribution. A circular aperture with radius $\Delta\nu$ is placed at the Fourier plane of the optical setup in order to stop down the resolution of the imaging system. Incoming light from a point source passes through a collimation lens L_C and produces on-axis collimated illumination over the optical setup. This collimated beam reaches the 1-D diffraction grating placed before the object. As we will see in the mathematical analysis, structured illumination is produced on the object by simply assuring the overlapping of the different diffraction orders of the 1-D grating over the imaged region of the object, that is, over the field of view provided by the imaging system.

Another way to understand structured illumination is in terms of tilted beams. In our case, tilted illumination is generated by each one of the collimated diffracted beams produced by the 1-D grating. This fact allows the transmission of different object frequency bands through the limited system aperture at the same instant. If a frequency band is shifted at the image space to its original position in the object's spectrum, then a 1-D superresolved image is synthesized. To obtain 2-D SR, the 1-D grating is placed on a rotary stage in order to allow off-axis illumination over the full 2-D frequency space of the object. But a relocation of each transmitted frequency band is needed for each rotation angle.

The present approach, called *rotating-grating approach*, performs the relocation using digital postprocessing of each recorded image for each orientation of the 1-D grating. Thus, the process can be carried out using continuous movement of the 1-D grating and storing in the computer memory a continuous sequence of images with the only limitation being the CCD recording time between consecutive images. Once the image sequence is recorded, digital postprocessing to achieve the SR effect can be performed using *a priori* information about the angular rotating-grating speed and its initial orientation. Angular rotation speed is needed to know the angular separation between two consecutive stored images. Then, it is possible to properly relocate each stored FT image in the digital decoding process. Initial line-grating orientation defines the starting point in the digital decoding process. Both angular rotation speed and initial orientation of the encoding grating can be obtained using calibration procedures prior to the SR approach.

In a way similar to the optical setup shown in Fig. 1 but splitting the illumination beam before it reaches the 1-D grating and reinserting it in off-axis mode at the recorded plane, an off-axis digital hologram can be recorded. Thus, the optical setup presented in Fig. 1 is capable of performing the superresolved imaging approach of both amplitude and phase object distribution because of the holographic recording process. To obtain this, the decoding must be produced over the diffraction order of the recorded hologram sequence. Let us call this modification of DIA *digital holographic imaging approach* (DHIA).

4. MATHEMATICAL ANALYSIS OF THE DIA APPROACH

In the following, a mathematical derivation of the rotating-grating approach for DIA is presented. In DIA, the on-axis collimated illumination beam impinges on the 1-D grating as is depicted in Fig. 1. The 1-D grating is placed on a platform that can be rotated along the system optical axis. Let us describe the amplitude distribution of such grating in terms of its Fourier coefficients:

$$U_0(x_0,y_0) = \sum_n C_n \exp\{-j2\pi n\nu_0[x_0 \cos\theta(t) + y_0 \sin\theta(t)]\}, \tag{1}$$

θ, ν_0 being the rotation angle and the basic frequency of the grating, respectively. Note that the rotation angle is a function of time [$\theta = \theta(t)$]. The amplitude distribution just infront of the input object is obtained by Fresnel propagation of Eq. (1). Thus, after some mathematic operations, one arrives at

$$U_z(x,y) = \sum_n C_n' \exp\{-j2\pi n\nu_0(x \cos\theta + y \sin\theta)\}, \tag{2}$$

where $C_n' = C_n(j\lambda z)\exp\{jkz\}\exp\{-j\pi\lambda z n^2\nu_0{}^2\}$ and z is the propagation distance.

Equation (2) describes the amplitude distribution under Fresnel approximation of a 1-D grating with new C_n' complex coefficients; this amplitude distribution illuminates the input object as

$$U_{IP}(x,y) = t(x,y)\sum_n C_n' \exp\{-j2\pi n\nu_0(x \cos\theta + y \sin\theta)\}, \tag{3}$$

where *IP* denotes input plane, and $t(x,y)$ represents the complex amplitude distribution of the input object. As we can see in Eq. (3), we have obtained structured illumination on the object in a way similar to the case when the encoding grating is attached to the object. But now, the new grating coefficients for the different diffraction orders are a function of the z propagation distance.

At the Fourier plane *FP* of the optical system, a FT of the previous amplitude distribution is obtained and multiplied by the circular limited aperture as

$$U_{FP}(u,v) = \left[\tilde{t}(u,v) \otimes \sum_n C_n{}' \delta(u + n\nu_0 \cos\theta, v + n\nu_0 \sin\theta)\right] \mathrm{circ}\left(\frac{\rho}{\Delta\nu}\right), \tag{4}$$

(u,v) being the spatial-frequency coordinates, ρ the polar coordinate in the frequency domain [defined as $\rho = \sqrt{u^2+\nu^2}$ (all computations are done in normalized units of λF where λ is the wavelength of the illumination and F is the focal length of the lenses], $\otimes$ the convolution operation, $\tilde{t}$ the FT of t, and $\Delta\nu$ the radius of the circular aperture.

Now, a second lens performs the second FT providing the following amplitude distribution at the output plane:

$$U_{Out}(x,y) = \sum_n C_n{}'[t(-x,-y)\exp\{j2\pi n\nu_0(x \cos\theta + y \sin\theta)\}] \otimes \mathrm{disk}(\Delta\nu r), \tag{5}$$

where $r = \sqrt{x^2+y^2}$ is the radial coordinate at the spatial domain and disk is the inverse FT of the circ aperture func-

tion. Then, the CCD computes the intensity distribution from Eq. (5) as

$$I_{Out}(x,y) = \sum_{n,m} C_n' C_m'^{*}\{[t(-x,-y) \times \exp\{j2\pi n\nu_0(x\cos\theta + y\sin\theta)\}] \otimes \mathrm{disk}(\Delta\nu r)\} \times \{[t(-x,-y)\exp\{j2\pi m\nu_0(x\cos\theta + y\sin\theta)\}]^{*} \otimes \mathrm{disk}(\Delta\nu r)\}, \quad (6)$$

which is digitally multiplied by the decoding grating. Assuming a digital decoding grating having the same basic frequency ν_0 as the encoding one and with a rotation angle $\varphi=\varphi(t)$ but $\varphi\neq\theta$, the final decoding intensity distribution is

$$I'_{Out}(x,y) = I_{Out}(x,y)\sum_k B_k \exp\{-j2\pi k\nu_0(x\cos\varphi + y\sin\varphi)\}. \quad (7)$$

Let us now observe the Fourier domain of Eq. (7). A little algebra provides

$$\widetilde{I'}(u,v) = \sum_{n,m,k} (\lambda z)^2 C_n C_m^{*} B_k \exp\{-j\pi\lambda z(n^2-m^2)\nu_0^2\} \times \left\{\tilde{t}(u,v)\left[\mathrm{circ}\left(\frac{\rho}{\Delta\nu}\right) \otimes \delta(u + n\nu_0\cos\theta, v + n\nu_0\sin\theta)\right]\right\} * \left\{\tilde{t}(u,v)\left[\mathrm{circ}\left(\frac{\rho}{\Delta\nu}\right) \otimes \delta(u + m\nu_0\cos\theta, v + m\nu_0\sin\theta)\right]\right\} \otimes \delta\{u - [(n-m)\cos\theta - k\cos\varphi]\nu_0, v - [(n-m)\sin\theta - k\sin\varphi]\nu_0\}, \quad (8)$$

where $*$ stands for the correlation operation.

Leaving aside constant coefficients, in order to obtain a superresolved image, two conditions must be fulfilled. The first states that the basic period of the encoding grating must be properly matched with the radius of the circular coherent transfer function (CTF) of the imaging system; that is, $\nu_0=2\Delta\nu$. If this condition is satisfied, a SA generation similar to that represented in Eq. (A2) can be obtained (see Appendix A). The second condition implies that the convolution with the last delta function must be centered at the Fourier domain. In such a case, the result is similar to that obtained in Eq. (A3) (see Appendix A). The second condition is accomplished if $(n-m)\cos\theta - k\cos\varphi=0$ and $(n-m)\sin\theta - k\sin\varphi=0$, which means that $\varphi=\theta+l\pi$, $l=0,1,2,\ldots$ and $k=n-m$.

The fact that $\varphi=\theta+l\pi$, $l=0,1,2,\ldots$ implies that the digital decoding grating must have the same line orientation as that used to perform the encoding process. The condition given by $k=n-m$ suggests that Eq. (8) must be separated into three different terms in order to analyze them separately; that is

$$\widetilde{I'}(u,v;\theta) = \sum_{\theta}\sum_{n,m}\sum_{k=n-m} (\lambda z)^2 C_n C_m^{*} B_k \exp\{-j\pi\lambda z(n^2-m^2)\nu_0^2\}\left\{\tilde{t}(u,v)\left[\mathrm{circ}\left(\frac{\rho}{\Delta\nu}\right) \otimes \delta(u + n\nu_0\cos\theta, v + n\nu_0\sin\theta)\right]\right\} * \left\{\tilde{t}(u,v)\left[\mathrm{circ}\left(\frac{\rho}{\Delta\nu}\right) \otimes \delta(u + m\nu_0\cos\theta, v + m\nu_0\sin\theta)\right]\right\} + \sum_{\theta}\sum_{n=m}\sum_{k\neq n-m} (\lambda z)^2 |C_n|^2 B_k \times \left\{\tilde{t}(u,v)\left[\mathrm{circ}\left(\frac{\rho}{\Delta\nu}\right) \otimes \delta(u + n\nu_0\cos\theta, v + n\nu_0\sin\theta)\right]\right\} * \left\{\tilde{t}(u,v)\left[\mathrm{circ}\left(\frac{\rho}{\Delta\nu}\right) \otimes \delta(u + n\nu_0\cos\theta, v + n\nu_0\sin\theta)\right]\right\} \otimes \delta(u + k\nu_0\cos\theta, v + k\nu_0\sin\theta) + \sum_{\theta}\sum_{n\neq m}\sum_{k\neq n-m} (\lambda z)^2 C_n C_m^{*} B_k \exp[-j\pi\lambda z(n^2-m^2)\nu_0^2]\left\{\tilde{t}(u,v)\left[\mathrm{circ}\left(\frac{\rho}{\Delta\nu}\right) \otimes \delta(u + n\nu_0\cos\theta, v + n\nu_0\sin\theta)\right]\right\} * \left\{\tilde{t}(u,v)\left[\mathrm{circ}\left(\frac{\rho}{\Delta\nu}\right) \otimes \delta(u + m\nu_0\cos\theta, v + m\nu_0\sin\theta)\right]\right\} \otimes \delta[u - (n-m-k)\nu_0\cos\theta, v - (n-m-k)\nu_0\sin\theta] = \widetilde{I'}_1(u,v;\theta) + \widetilde{I'}_2(u,v;\theta) + \widetilde{I'}_3(u,v;\theta). \quad (9)$$

Note that the indexes (n,m,k) run over all possible values. The first term, $\widetilde{I'}_1(u,v;\theta)$, corresponding to the index combination of $k=n-m$, $\forall n,m$, yields the SR effect when the overall process is performed, that is, provided that both encoding and decoding gratings are rotated to completely ensure the 2-D full coverage of the object's spectrum. This condition is produced when the rotation angle is at least 180°: $\theta=0°$ *to* 180°. Then, the CTF of the imaging system is convolved with a combination of delta functions that implies the generation of a SA. We can rewrite

this first term as

$$\widetilde{I'}_1(u,v;\theta) = (\lambda z)^2 \sum_{n,m} \sum_{k=n-m} C_n C_m{}^* B_k \exp[-j\pi\lambda z(n^2-m^2)\nu_0{}^2] \times [\tilde{t}(u,v)SA_n(u,v)] * [\tilde{t}(u,v)SA_m(u,v)], \quad (10)$$

where

$$SA_n(u,v) = \sum_{\theta} \mathrm{circ}\left(\frac{\rho}{\Delta\nu}\right) \otimes \delta(u + n\nu_0 \cos\theta, v + n\nu_0 \sin\theta). \quad (11)$$

Comparing Eq. (10) with the desired result for DIA [Appendix A, Eq. (A3)], they coincide, provided that

$$(\lambda z)^2 C_n C_m{}^* B_{n-m} \exp[-j\pi\lambda z(n^2-m^2)\nu_0{}^2] = A_n A_m{}^* \quad (12)$$

The second term, $\widetilde{I'}_2(u,v;\theta)$, is due to the index combination $n=m$, $\forall k \neq n-m$. For simpler analysis, this second term can be separated into two groups, those corresponding to the index combinations given by $n=m=0$ and $n=m\neq 0$:

$$\begin{aligned}\widetilde{I'}_2(u,v;\theta) = {} & \sum_{\theta} \sum_{n=m=0} \sum_{k\neq n-m} (\lambda z)^2 |C_0|^2 B_k \\ & \times \left[\tilde{t}(u,v)\mathrm{circ}\left(\frac{\rho}{\Delta\nu}\right)\right] * \left[\tilde{t}(u,v)\mathrm{circ}\left(\frac{\rho}{\Delta\nu}\right)\right] \\ & \otimes \delta(u + k\nu_0 \cos\theta, v + k\nu_0 \sin\theta) \\ & + \sum_{\theta} \sum_{n=m\neq 0} \sum_{k\neq n-m} (\lambda z)^2 |C_n|^2 B_k \\ & \times \left\{\tilde{t}(u,v)\left[\mathrm{circ}\left(\frac{\rho}{\Delta\nu}\right) \otimes \delta(u + n\nu_0 \cos\theta, v + n\nu_0 \sin\theta)\right]\right\} \\ & * \left\{\tilde{t}(u,v)\left[\mathrm{circ}\left(\frac{\rho}{\Delta\nu}\right) \otimes \delta(u + n\nu_0 \cos\theta, v + n\nu_0 \sin\theta)\right]\right\} \\ & \otimes \delta(u + k\nu_0 \cos\theta, v + k\nu_0 \sin\theta). \end{aligned} \quad (13)$$

The first addend of Eq. (13) causes a high distortion in the final superresolved image. Basically, it implies that the central frequency band of the object's spectrum is positioned at the frequencies defined by the diffraction orders of the decoding grating. And because most of the object's spectrum intensity corresponds to the DC term, the first addend in Eq. (13) implies significant distortion in the decoded spectrum. As we can see in such first term, the object's spectrum is band limited by the system aperture and the autocorrelation result is centered at the positions related to the diffraction orders of the decoding grating for each rotation angle θ. When the complete rotation process is performed, that is, when θ goes from 1° to 180°, the DC term follows a circle at the Fourier domain. This circle causes a high distortion in the superresolved image when FT is computed.

In addition to the previous distortion term, the second addend in Eq. (13) also distorts the final image. It corresponds with the autocorrelation ($n=m\neq 0$) of the frequency bands selected by the ±1st diffraction orders of the encoding grating. These autocorrelation terms contribute to increase the distortion of the final superresolved image.

Finally, the third term $\widetilde{I'}_3(u,v;\theta)$ in Eq. (9), given by the remaining index combination $n\neq m$, $\forall k\neq n-m$, means the generation of cross correlation terms between different frequency bands corresponding with high-frequency slots in the object's spectrum. This contribution to image distortion will be lower when compared with the previous ones:

$$\begin{aligned}\widetilde{I'}_3(u,v;\theta) = {} & \sum_{\theta} \sum_{n\neq m} \sum_{k\neq n-m} (\lambda z)^2 C_n C_m{}^* B_k \exp[-j\pi\lambda z(n^2 - m^2)\nu_0{}^2] \\ & \times \left\{\tilde{t}(u,v)\left[\mathrm{circ}\left(\frac{\rho}{\Delta\nu}\right) \otimes \delta(u + n\nu_0 \cos\theta, v + n\nu_0 \sin\theta)\right]\right\} * \left\{\tilde{t}(u,v) \times \left[\mathrm{circ}\left(\frac{\rho}{\Delta\nu}\right) \otimes \delta(u + m\nu_0 \cos\theta, v + m\nu_0 \sin\theta)\right]\right\} \\ & \otimes \delta[u - (n-m-k)\nu_0 \cos\theta, v - (n-m-k)\nu_0 \sin\theta]. \end{aligned} \quad (14)$$

The previous mathematical development shows that an additional digital postprocessing is needed to obtain a high-quality, distortion-free final image. Such additional process consists of the addition into one image of all the FT of each stored CCD intensity image that was obtained for each θ angle orientation of the encoding grating. Let us name each one of such Fourier domain images *partial spectral image*. From Eq. (6), it is possible to derive the expression of each partial spectral image. After that, the spectral distribution resulting from the addition of all the partial spectral images is replicated to the positions defined by the nonzeroth diffraction orders of the decoding grating:

$$\begin{aligned}\widetilde{I'}(u,v;\theta) = {} & \sum_{\theta} \sum_{n,m} \sum_{k\neq 0} (\lambda z)^2 C_n C_m{}^* B_k \exp[-j\pi\lambda z(n^2 - m^2)\nu_0{}^2] \\ & \times \left\{\tilde{t}(u,v)\left[\mathrm{circ}\left(\frac{\rho}{\Delta\nu}\right) \otimes \delta(u + n\nu_0 \cos\theta, v + n\nu_0 \sin\theta)\right]\right\} * \left\{\tilde{t}(u,v)\left[\mathrm{circ}\left(\frac{\rho}{\Delta\nu}\right) \otimes \delta(u + m\nu_0 \cos\theta, v + m\nu_0 \sin\theta)\right]\right\} \\ & \otimes \delta[u - (n-m-k)\nu_0 \cos\theta, v - (n-m-k)\nu_0 \sin\theta]. \end{aligned} \quad (15)$$

Eq. (15) can also be divided into two terms according to the analysis performed in Eq. (9):

$$\widetilde{I'}(u,v;\theta) = \sum_{\theta}\sum_{n=m}\sum_{k\neq 0}(\lambda z)^2|C_n|^2B_k\left\{\tilde{t}(u,v)\left[\mathrm{circ}\left(\frac{\rho}{\Delta\nu}\right)\otimes\delta(u + n\nu_0\cos\theta, v + n\nu_0\sin\theta)\right]\right\} * \left\{\tilde{t}(u,v)\times\left[\mathrm{circ}\left(\frac{\rho}{\Delta\nu}\right)\otimes\delta(u + n\nu_0\cos\theta, v + n\nu_0\sin\theta)\right]\right\} \otimes \delta(u - k\nu_0\cos\theta, v - k\nu_0\sin\theta) + \sum_{\theta}\sum_{n\neq m}\sum_{k\neq 0}(\lambda z)^2C_nC_m{}^*B_k\exp[-j\pi\lambda z(n^2 - m^2)\nu_0{}^2]\left\{\tilde{t}(u,v)\left[\mathrm{circ}\left(\frac{\rho}{\Delta\nu}\right)\otimes\delta(u + n\nu_0\cos\theta, v + n\nu_0\sin\theta)\right]\right\} * \left\{\tilde{t}(u,v)\left[\mathrm{circ}\left(\frac{\rho}{\Delta\nu}\right)\otimes\delta(u + m\nu_0\cos\theta, v + m\nu_0\sin\theta)\right]\right\} \otimes \delta(u - k\nu_0\cos\theta, v - k\nu_0\sin\theta). \quad (16)$$

The first addend in Eq. (16) is exactly the same as the one represented as $\widetilde{I'}_2(u,v;\theta)$ in Eq. (9). Thus, the two main distortion factors of the final superresolved image [Eq. (13)] can be avoided by simple subtraction in a digital postprocessing. On the other hand, the second addend in Eq. (16) also removes some of the distortion terms presented in $\widetilde{I'}_3(u,v;\theta)$. Equation (14) represents the generation of cross correlation terms ($n \neq m$) between different frequency bands. Such distortion terms are duplicated to the positions defined by $k \neq n-m$. The second addend in Eq. (16) also implies the generation of cross correlation terms ($n \neq m$) but placed at the nonzeroth diffraction orders ($k \neq 0$) of the decoding grating. So, those distortion terms generated in Eq. (14) and placed at the nonzeroth diffraction orders will also be removed by the digital postprocessing subtraction. Only the cross correlation terms located at the zeroth hologram order will remain. But those terms will have low distortion contribution because they come from the cross correlation ($n \neq m$) of different frequency bands in the object's spectrum:

$$\widetilde{I'}_{RE}(u,v;\theta) = \sum_{\theta}\sum_{n\neq m}(\lambda z)^2C_nC_m{}^*B_0\exp[-j\pi\lambda z(n^2 - m^2)\nu_0{}^2]\times\left\{\tilde{t}(u,v)\left[\mathrm{circ}\left(\frac{\rho}{\Delta\nu}\right)\otimes\delta(u + n\nu_0\cos\theta, v + n\nu_0\sin\theta)\right]\right\} * \left\{\tilde{t}(u,v)\left[\mathrm{circ}\left(\frac{\rho}{\Delta\nu}\right)\otimes\delta(u + m\nu_0\cos\theta, v + m\nu_0\sin\theta)\right]\right\}, \quad (17)$$

where $\widetilde{I'}_{RE}(u,v;\theta)$ is the remaining distortion contribution to the frequency domain.

5. MATHEMATICAL ANALYSIS OF THE DHIA APPROACH

In a way similar to the theoretical analysis presented for DIA, a theoretical foundation for DHIA can be formulated, the only consideration being to introduce a coherent reference beam over the CCD output plane in the recording process. Thus, instead of repeating again the whole mathematical analysis, the following summarizes the key equations for DHIA and presents some figures to help understand the contribution of every term. In DHIA, the amplitude distribution at the output plane comes from the addition of Eq. (5) with a linear phase factor representing the coherent off-axis reference beam:

$$U'_{Out}(x,y) = \sum_n C_n{}'\{t(-x,-y)\exp[j2\pi n\nu_0(x\cos\theta + y\sin\theta)]\} \otimes \mathrm{disk}(\Delta\nu r) + R\exp[-j2\pi\mu_0 x], \quad (18)$$

μ_0 and R being the bias carrier frequency and the constant amplitude of the reference beam, respectively. For a given rotation angle θ of the encoding grating, the CCD computes the intensity distribution that can be separated into three terms corresponding by analogy to the three different diffraction orders of the recorded hologram. But the interest in the DHIA lies in the −1st hologram order because it has information about the complex amplitude distribution of the input object. Let us call this term $I_2(x,y)$. So, provided that the carrier frequency of the holographic recording should be high enough to ensure the nonoverlapping between the zeroth-order term and the first diffraction order of the recorded hologram—that is, $\mu_0 \geqslant 3\Delta\nu$—the −1st diffraction can be filtered and centered at the Fourier domain. Thus, it is possible to apply the rotating grating approach to such spectral distribution.

At this point, some comments must be introduced. First, note that the zeroth-order term of the recorded hologram is exactly the same as the one that was analyzed in DIA [Eq. (6)]. The only difference comes from the addition of a constant originated from the reference beam. Thus, a procedure similar to DIA can be performed over this term. Second, and going ahead with the digital decoding process, it is convenient to our superresolved purposes that the frequency bands selected by the encoding grating contiguous bands. This can be achieved by proper selection of the basic frequency ν_0 of the encoding grating ($\nu_0 = 2\Delta\nu$). And third, θ must run between at least 0 and 180° to obtain a final 2-D superresolved image.

After recovering the −1st hologram diffraction order, a similar procedure to that which is shown for DIA is performed taking into account at least 180° in the rotation grating approach. Equation (19) below summarizes this process, where no Fresnel propagation is in principle computed for the decoding grating, and a different rotation angle $\varphi \neq \theta$ is again considered:

$$\tilde{I}_2(u,v) = R^*\sum_{n,\theta}\sum_{k,\varphi}C_n{}'B_k\left\{[\tilde{t}(u,v)\otimes\delta(u + n\nu_0\cos\theta, v + n\nu_0\sin\theta)]\mathrm{circ}\left(\frac{\rho}{\Delta\nu}\right)\right\}\otimes\delta(u + k\nu_0\cos\varphi, v + k\nu_0\sin\varphi)$$

$$= R^* \sum_{\theta,\varphi} \sum_{n,k} C'_n B_k \left\{ \tilde{t}(u,v) \left[\mathrm{circ}\left(\frac{\rho}{\Delta\nu} \right) \otimes \delta(u - n\nu_0 \cos\theta, v - n\nu_0 \sin\theta) \right] \right\} \otimes \delta[u + (n\cos\theta + k\cos\varphi)\nu_0, v + (n\sin\theta + k\sin\varphi)\nu_0]. \quad (19)$$

To obtain the SR effect, the convolution with the last delta function must be centered at the Fourier domain. This is accomplished if $n\cos\theta + k\cos\varphi = 0$ and $n\sin\theta + k\sin\varphi = 0$, which means that $\varphi = \theta + m\pi$, $m = 0, 1, 2\ldots$ and $k = -n$. The fact that $\varphi = \theta + l\pi$ and $l = 0, 1, 2\ldots$ forces the digital grating to have the same line orientation as the encoding grating, that is, both gratings must be parallel. Now, it is more convenient to separate Eq. (19) into three different terms and analyze them separately:

$$\begin{aligned} \tilde{I}_2(u,v) &= R^* \sum_{\theta} \sum_{n} \sum_{k=-n} C'_n B_{-n} \left\{ \tilde{t}(u,v) \left[\mathrm{circ}\left(\frac{\rho}{\Delta\nu} \right) \otimes \delta(u - n\nu_0 \cos\theta, v - n\nu_0 \sin\theta) \right] \right\} \\ &+ R^* \sum_{\theta} \sum_{n=0} \sum_{k\neq -n} C'_0 B_k \left\{ \tilde{t}(u,v) \mathrm{circ}\left(\frac{\rho}{\Delta\nu} \right) \right\} \otimes \delta(u + k\nu_0 \cos\theta, v + k\nu_0 \sin\theta) \\ &+ R^* \sum_{\theta} \sum_{n\neq 0} \sum_{k\neq -n} C'_n B_k \left\{ \tilde{t}(u,v) \left[\mathrm{circ}\left(\frac{\rho}{\Delta\nu} \right) \otimes \delta(u - n\nu_0 \cos\theta, v - n\nu_0 \sin\theta) \right] \right\} \otimes \delta(u + (n + k)\nu_0 \cos\theta, v + (n + k)\nu_0 \sin\theta) \\ &= \tilde{T}_1(u,v) + \tilde{T}_2(u,v) + \tilde{T}_3(u,v). \end{aligned} \quad (20)$$

Note that both (n,k) indexes continue taking all possible values. The first term $\tilde{T}_1(u,v)$, corresponding to the indexes combination $k = -n\ \forall n$, yields the SR effect when the rotating grating process is performed. In such a case, we can see that the circular limited aperture of the system is now convolved with a combination of delta functions that implies the generation of a SA. Figure 2 shows for an easy interpretation the SA generation considering that both gratings have three diffraction orders $(n,k = -1,0,+1)$. The gray circles represent the CTF of the imaging system, and the black point at the spectrum's center represents the DC term in the object's spectrum. As a consequence of the continuous overlapping for each decoding grating orientation, the central frequency band is reinforced.

So, in order to obtain a well-balanced final image, an equalization of this central part is needed. We can rewrite the first term of Eq. (20) as

$$\tilde{T}_1(u,v) = \tilde{t}(u,v) \otimes R^* \sum_{n} C'_n B_{-n} SA_n(u,v), \quad (21)$$

where

$$SA_n(u,v) = \sum_{\theta} \mathrm{circ}\left(\frac{\rho}{\Delta\nu} \right) \otimes \delta(u + n\nu_0 \cos\theta, v + n\nu_0 \sin\theta) \quad (22)$$

is the generated SA. Comparing Eq. (21) with the desired result for DHIA [see Appendix A, Eq. (A1)], the result coincides, provided that

$$j\lambda z \exp(jkz) R^* C_n B_{-n} \exp[-j\pi\lambda z n^2 \nu_0^2] = A_n. \quad (23)$$

The second term $\tilde{T}_2(u,v)$ is due to the indexes combination of $n = 0$, $\forall k \neq -n$ as we can see in

$$\tilde{T}_2(u,v) = R^* \sum_{\theta} \sum_{n=0} \sum_{k\neq -n} C'_0 B_k \left[\tilde{t}(u,v) circ\left(\frac{\rho}{\Delta\nu} \right) \right] \otimes \delta(u + k\nu_0 \cos\theta, v + k\nu_0 \sin\theta). \quad (24)$$

Taking a detailed look, the term in the square brackets in Eq. (24) implies that the central part of the object's spectrum is filtered by the limited system aperture and centered at the positions defined by the diffraction orders of the decoding grating $(k \neq 0)$. As in DIA, the decoding produces something similar to a circle at the Fourier domain by dragging the DC term of the object's spectrum. This fact is depicted in Fig. 3 assuming again that both gratings have three diffraction orders $(n = -1,0,+1)$. The enhanced black circle is generated when the overall rotating grating process is done and causes high distortion when the FT is produced to obtain SR.

In addition to the $\tilde{T}_2(u,v)$ term, the third term $\tilde{T}_3(u,v)$ corresponding to the combination of the indexes of $n \neq 0$, $\forall k \neq -n$ also distorts the final image:

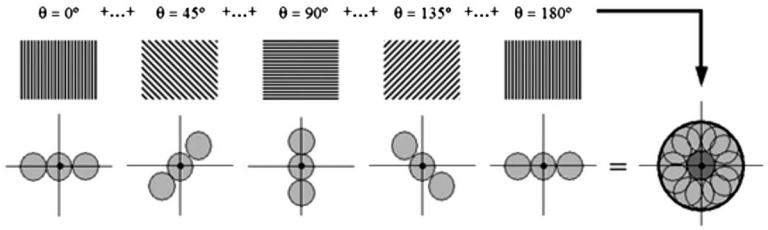


Fig. 2. SA generated using DHIA. The smaller circles represent the region of the frequency space that is observable through the conventional system aperture in comparison with the right-hand figure, which shows the SA (external black circle) achieved using the DHIA approach.

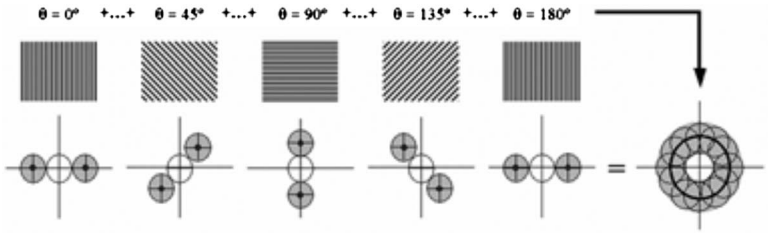


Fig. 3. Distortion generated in DHIA. The object's spectral DC term is represented by a black point at the center of the laterally positioned gray circles and was generated by dragging the enhanced black circle represented in the SA after performance of the DHIA approach.

$$\tilde{T}_3(u,v) = R^* \sum_{\theta} \sum_{n\neq 0} \sum_{k\neq -n} C_n' B_k \left\{ \tilde{t}(u,v) \left[\mathrm{circ}\left(\frac{\rho}{\Delta\nu} \right) \otimes \delta(u - n\nu_0 \cos\theta, v - n\nu_0 \sin\theta) \right] \right\} \otimes \delta(u + (n+k)\nu_0 \cos\theta, v + (n+k)\nu_0 \sin\theta). \tag{25}$$

In Eq. (25), the square-brackets convolution selects a new contiguous frequency band of the object's spectrum. This additional object information is centered over the diffraction orders of the decoding grating with the particularity that they are different from the initial ones ($k \neq n$).

Figure 4 depicts an example given by ($n=1, k=0, 1$) and for vertical line grating orientation ($\theta=0°$). We can see that the selected object frequency band is the right one [Fig. 4(a)], and it is centered at the left and zero order positions [Fig. 4(b)]. This means that Eq. (25) has two contributions for each pair of values ($n \neq 0, \theta$). The first one corresponds with the relocation given by $k=n$, that is, the left circle in Fig. 4(b). Note that when the rotating grating process is performed, the left frequency band describes a circle in a similar way as that represented in Eq. (24).

The second contribution corresponds to the relocation given by $k=0$, that is, at the central region of the Fourier domain. This division is very important and suggests that Eq. (25) may be separated into two terms in accordance with the previous comment:

$$\tilde{T}_3(u,v) = R^* \sum_{\theta} \sum_{n\neq 0} \sum_{\substack{k\neq -n \\ k=n}} C_n' B_k \left\{ \tilde{t}(u,v) \left[\mathrm{circ}\left(\frac{\rho}{\Delta\nu} \right) \otimes \delta(u - n\nu_0 \cos\theta, v - n\nu_0 \sin\theta) \right] \right\} \otimes \delta(u + (n+k)\nu_0 \cos\theta, v + (n+k)\nu_0 \sin\theta)$$

$$+ R^* \sum_{\theta} \sum_{n\neq 0} \sum_{\substack{k\neq -n \\ k=0}} C_n' B_0 \left\{ \tilde{t}(u,v) \left[\mathrm{circ}\left(\frac{\rho}{\Delta\nu} \right) \otimes \delta(u - n\nu_0 \cos\theta, v - n\nu_0 \sin\theta) \right] \right\} \otimes \delta(u + n\nu_0 \cos\theta, v + n\nu_0 \sin\theta). \tag{26}$$

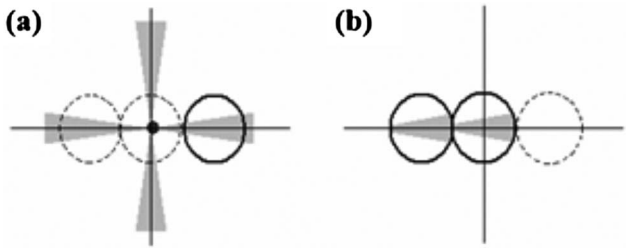


Fig. 4. (a) Overall object spectrum and selection of the right frequency band corresponding to the combination (n=1, $\theta=0°$), and (b) its relocation during the decoding process at the left and central position given by $k \neq -1$.

Once again, the exposed mathematical foundation suggests an additional digital postprocessing to obtain a high-quality superresolved image free of distortion when DHIA is performed. In that sense, mathematical derivation analogous to that performed for DIA can be performed for DHIA.

6. COMPUTATIONAL SIMULATION FOR DIA

The proposed rotating grating approach is investigated by a simulation process with a double aim. On one hand, it implies the validation of DIA depicted in Fig. 1 and theoretically developed in Section 4. On the other hand, it shows the required digital processing needed to yield a high-quality superresolved image after performing DIA.

A picture of the central part of a United States Air Force (USAF) resolution test target (see Fig. 13 below) is used to test the capabilities of the DIA. The encoding and decoding gratings used in the simulations are sinusoidal, and a resolution gain factor of 3 will be achieved. To simulate the noncontact effect of the encoding grating onto the object at the input plane, we use a process of double digital fractional FT as described in Ref. [51]. Figure 5 shows in (a) the low-resolution image of the object and its FT, and in (b) the high-resolution image (desired result) obtained with an expanded pupil that triples the low-resolution one. The dashed white circle in Fig. 5(b) represents the CTF of the optical system.

Then, we perform the SR approach where the USAF input object is subjected to the encoding process. In this, the encoding grating is rotated from 0° to 180° in 1° steps and a sequence of 180 images is stored in the computer memory. To obtain the SR effect, we need to perform the digital decoding stage, in which each one of the 180 stored images is digitally multiplied by a decoding grating with the same line orientation (same rotation angle) as that used in the encoding process to store each particular image.

The whole decoding procedure is depicted in Fig. 6(a). The central dashed circle represents the limited system

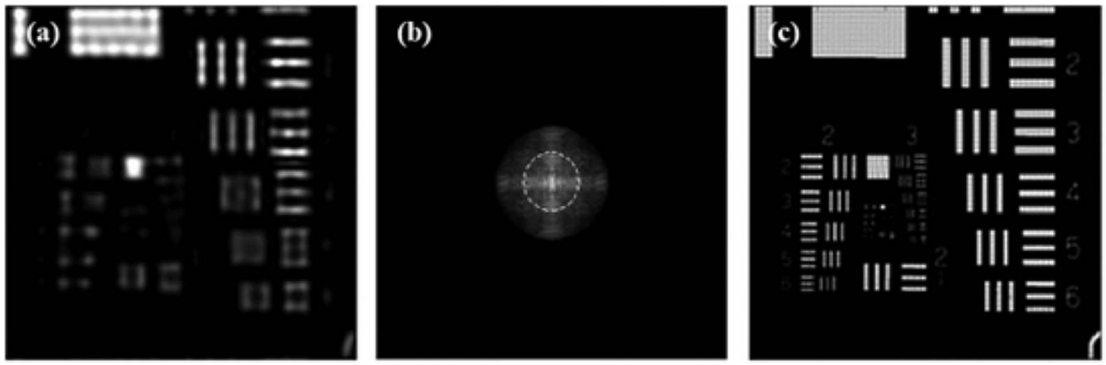


Fig. 5. (a) Low-resolution image of the input object provided by the system without the approach present, (b) its FT, and (c) the desired high-resolution image (that obtained with an aperture that triples the original one).

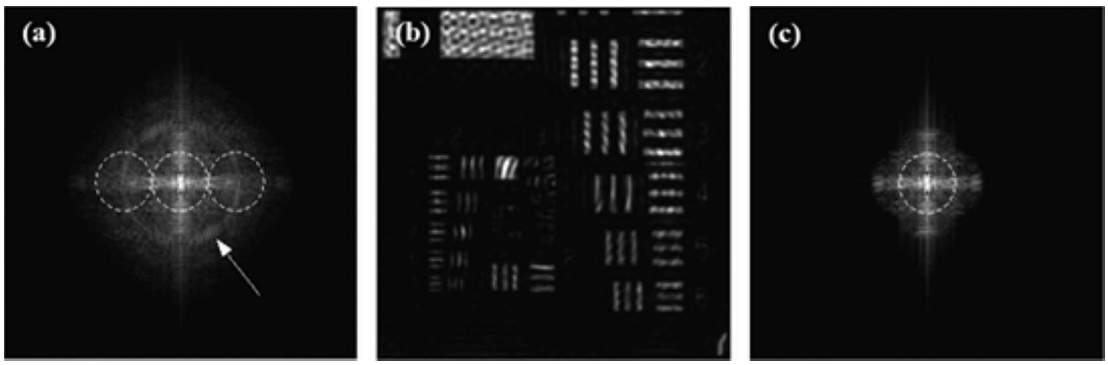


Fig. 6. (a) Total spectrum when digital decoding is produced, (b) FT of the image shown in (a), and (c) FT of the whole intensity distribution recorded at the CCD.

aperture for the coherent case, and the left and right dashed circles represent the pupil function centered at the ±1st diffraction orders of the digital decoding grating when the grating lines are vertical. Obviously, for each rotation angle of the encoding process, both lateral dashed circles turn around the central one generating the 2-D spectral distribution. But at the same instant, the zeroth order of each recorded image is also placed at the positions defined by the decoding grating diffraction orders. This generates a circle at the Fourier domain. That circle is indicated by a white arrow in Fig. 6(a), and it is responsible for a high distortion in the reconstructed image, as we can see in Fig. 6(b).

According to the theory, the decoding process produces the SR effect by properly replacing the different correlation terms due to the structured illumination [Eq. (10)], but introduces high distortion because it duplicates several times other correlation terms in the wrong places [Eqs. (13) and (14)]. To avoid this undesired distortion, a digital postprocessing is necessary. We add all the single stored images together and perform an operation similar to the previous digital decoding process, but taking into account only the ±1st diffraction orders of the digital decoding grating (not the zeroth order). The addition of all the single recorded images is depicted in Fig. 6(c), and the new digital procedure is shown in Fig. 7(a), where we can see the dragged circle produced by the DC term [indicated by the arrow in Fig. 6(a)] in a most obvious way.

Now, if we subtract Fig. 7(a) from Fig. 6(a)—first providing that the intensity of both images has been previously equalized—we obtain a "clean" superresolved spectrum where most of the distortion is avoided. The result is

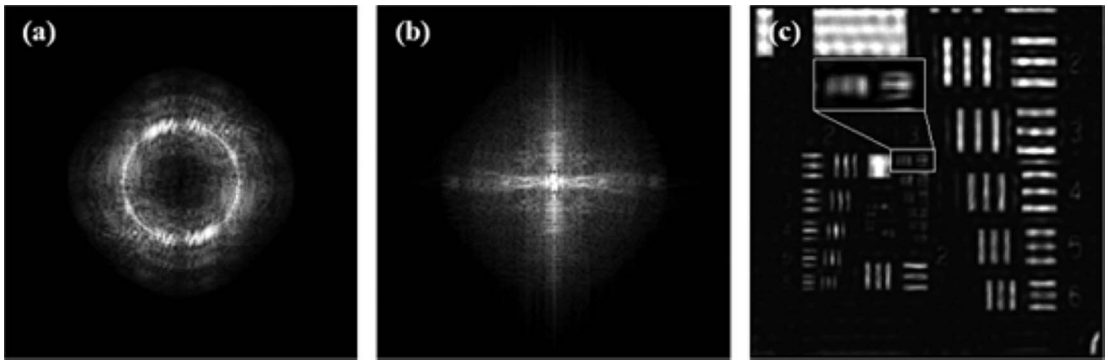


Fig. 7. (a) Dragged DC term of the diffraction orders of the digital decoding grating, (b) final synthesized spectrum, and (c) FT of the image shown in (b) that shows the final superresolved image.

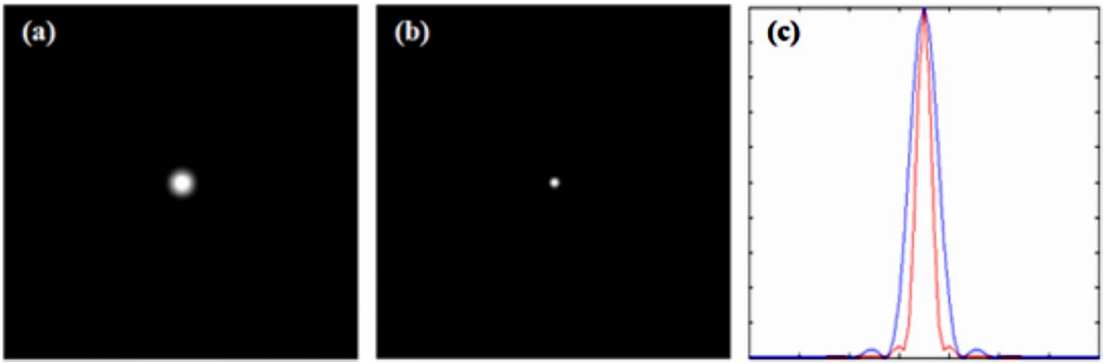


Fig. 8. (Color online) (a) PSF intensity without the present approach, (b) PSF intensity with the present approach, and (c) cross section of the PSF depicted in (a) and (b) that shows the improvement in resolution.

depicted in Fig. 7(b). Finally, by FT of the spectrum represented in Fig. 7(b), the final superresolved image is obtained in (c). Note that not only the distortion introduced by the DC term has been removed, but also the distortion due to the autocorrelation of the frequency bands selected by the ±1st diffraction orders of the encoding grating. Thus, only the terms represented in Eq. (17) provide a less significant distortion that results in the little difference between Fig. 5(c) and Fig. 7(c).

Simulation results are also provided in Fig. 8 for the case when the input object is a delta function. In such a case, we obtain the intensity point-spread function (PSF) of the system. Figures 8(a) and 8(b) depict the intensity PSF without and with the present approach, respectively, and Fig. 8(c) shows a comparative cross section between them where the blue (outer) and red (inner) plotted curves depict the cross section without and with the presented approach, respectively.

7. COMPUTATIONAL SIMULATION FOR DHIA

In this section, a simulation process for DHIA is presented. Again, both encoding and decoding gratings have three diffraction orders and a resolution improvement factor of 3 will be aimed for. DHIA has been tested in simulation for two different objects: the central part of a negative USAF resolution test target image and a Barbara image. Figure 9 shows a picture of both objects, their FTs, and the low-resolution image obtained with the limited aperture imaging system and without using the presented approach. Once again, the white circle in Figs. 9(b)

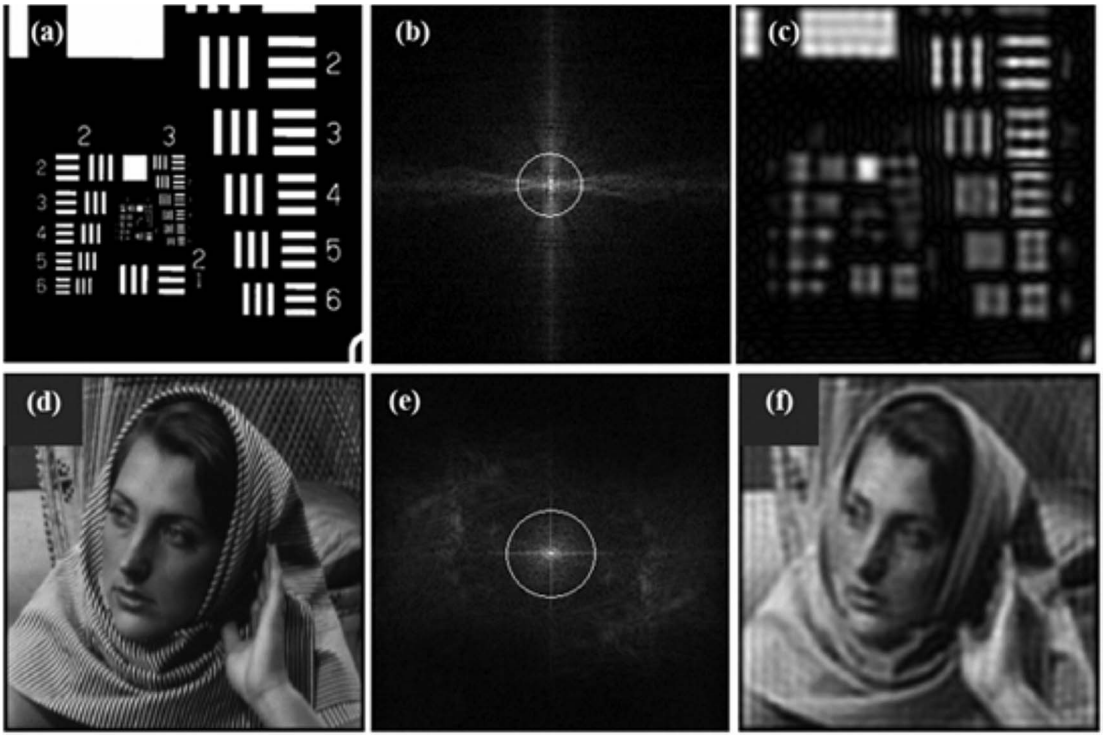


Fig. 9. (a), (d) show the input objects: USAF resolution test and Barbara images, respectively; (b), (e) Fourier transformations of (a) and (d), where the white circle represents the limited system aperture; and (c), (f) the low-resolution images obtained taking into account an imaging system with the previous limited aperture.

and 9(e) depicts the CTF of the imaging system. The radius of the CTF has been adjusted for each input object in such a way that the SR effect will be clearly noticeable.

Now, the simulation process is performed with the particularity of the introduction of a constant coherent reference beam at the output plane. Figure 10 shows an example of the simulated holograms in both spatial and Fourier domains. Unlike in the mathematical development, the reference beam used in the simulation analysis has a bias carrier frequency in the two orthogonal directions (μ_0, ν_0), and the condition to fulfill is $\sqrt{\mu_0^2+\nu_0^2} \geqslant 3\Delta\nu$ to avoid the overlapping of the ±1st diffracted orders with the central one. Figure 11(d) depicts this situation graphically.

Then, the −1st diffraction order of each stored hologram is filtered, replaced at the center of the Fourier domain, and multiplied by a digital decoding grating with the same orientation as that used in the encoding process. Figures 11(a) and 11(d) image the results at the Fourier domain when the rotating grating process is performed. We can see the dragged circle generated as a consequence of the objects spectrum DC term. Moreover, as we had commented previously, the central part of the object's spectrum (that corresponding with the zeroth order of the decoding grating) is reinforced in the decoding process by multiple overlapping of itself, and an equalization must be made [Figs. 11(b) and 11(e)]. Finally, Figs. 11(c) and 11(f) depict the reconstructed image by FT of (b) and (e), respectively. We can see the high distortion introduced as a consequence of the undesired frequency bands that are replicated at the Fourier domain in the performance of our approach and which correspond with Eqs. (24) and (26).

To obtain a good-quality final image, we perform an additional digital postprocessing similar to that presented in the DIA case. Thus, all the filtered and centered −1st hologram orders are added into one, and this resultant spectral distribution is replicated to the ±1st diffraction order positions of the digital decoding grating for the 180° of the decoding rotating process. Figures 12(a) and 12(d) show this process, where we can see the dragged circle produced by the DC term in a most obvious way. Now, if

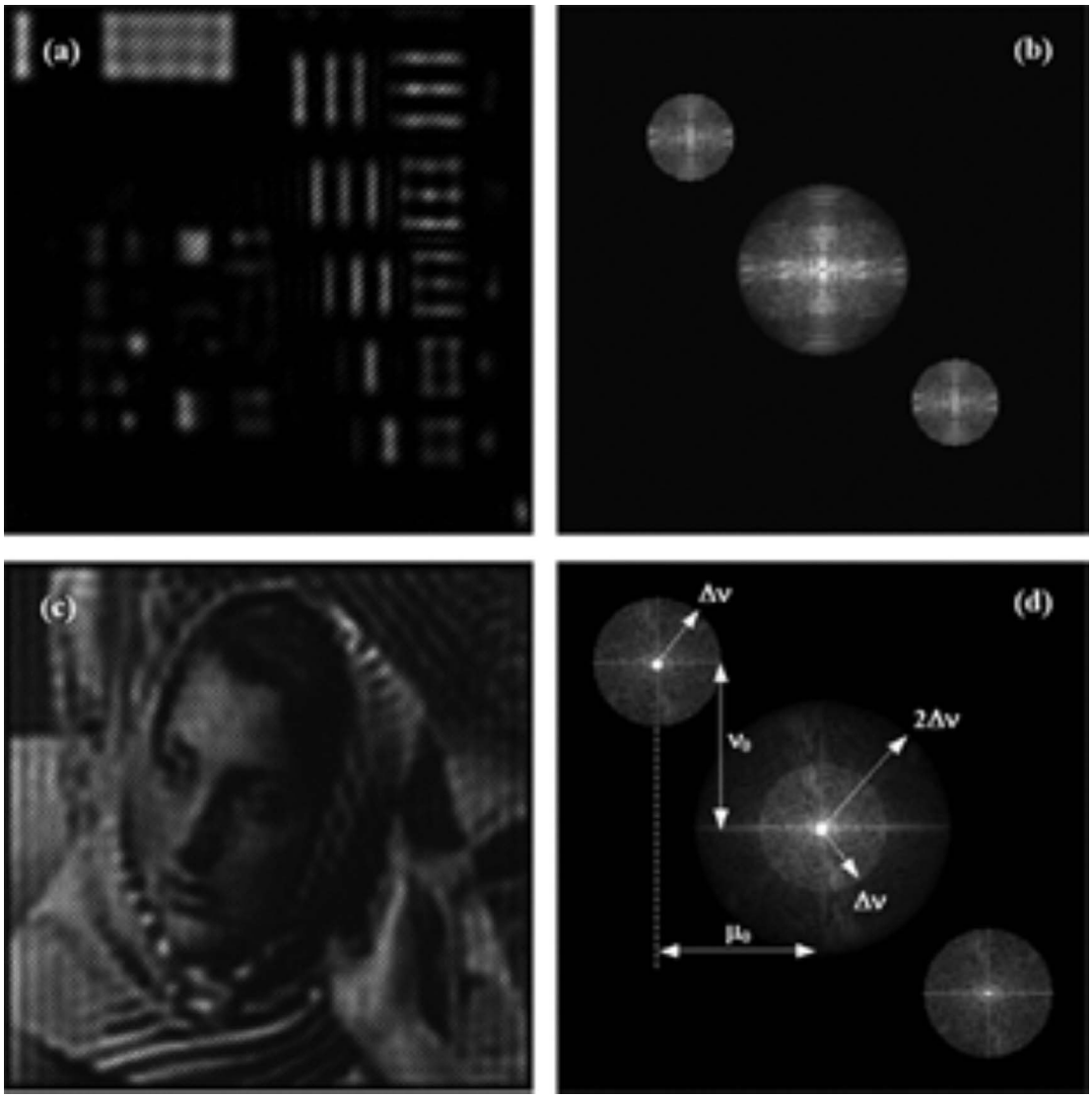


Fig. 10. (a), (c) Simulated holograms for USAF and Barbara objects, and (b), (d) their Fourier transformations, respectively. The central pixel has been blocked to enhance the visibility of the overall image.

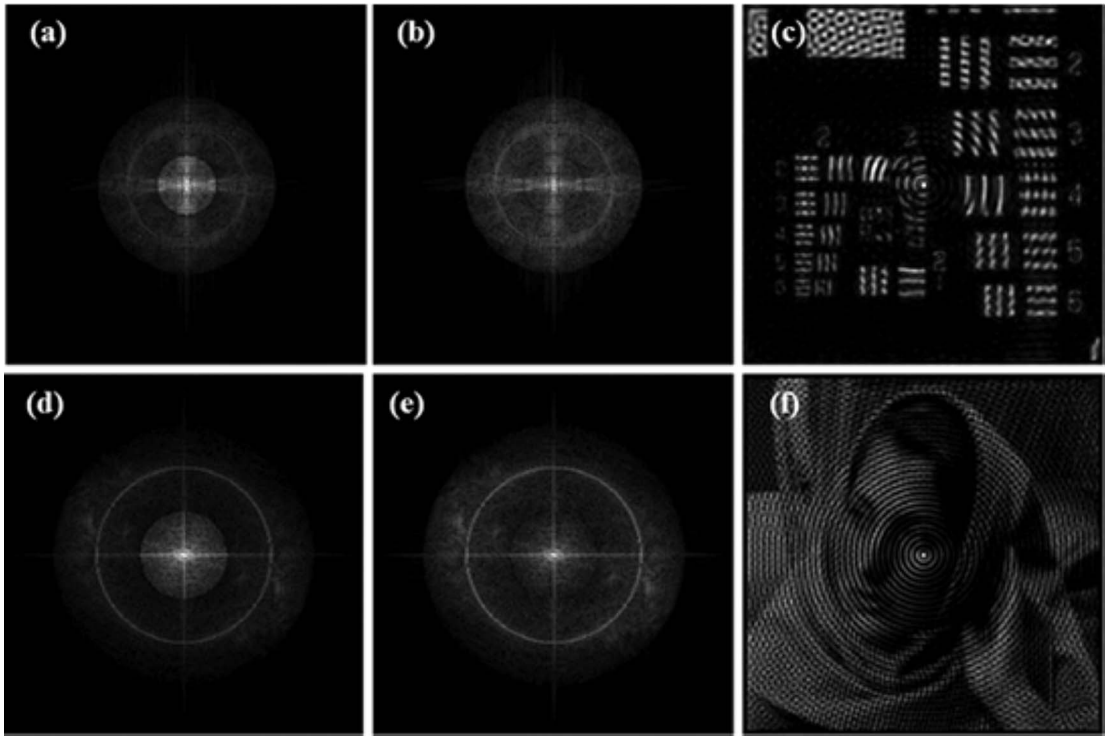


Fig. 11. (a), (d) Raw result of the present approach, and (b), (e) equalized central part of the object spectrum. (c), (f) show the distorted final image.

we subtract these Fourier distributions from Figs. 11(b) and 11(e), respectively—and provided that the intensity of both pair of images has been previously equalized—we avoid most of the distortion in the synthesized spectrum. The final generated SA without the DC term is depicted in Figs. 12(b) and 12(e). Finally, the final superresolved image is obtained by FT [Figs. 12(c) and 12(f)].

Note that not only the distortion introduced by the DC term has been removed [Eq. (24)], but also the distortion provided by the frequency bands selected by the ±1st dif-

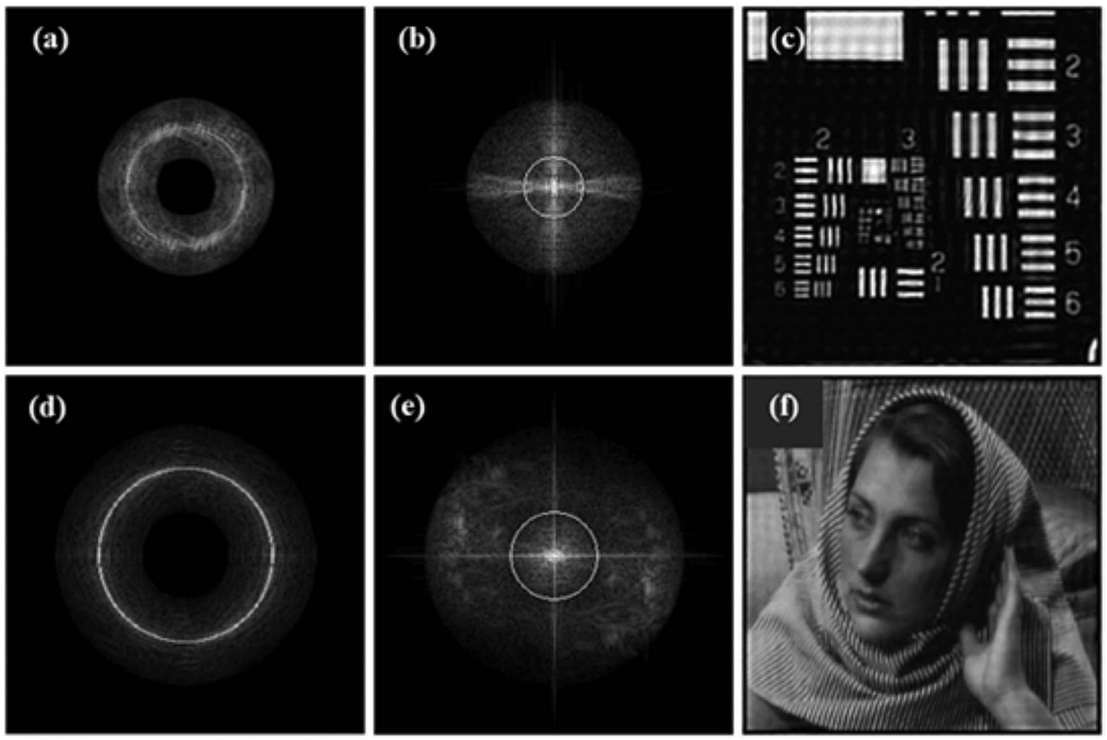


Fig. 12. (a), (d) Digital procedure to avoid distortion; (b), (e) generated SA in comparison with the real one (white circle); and (c), (f) final superresolved images obtained with the present approach.

fraction orders of the encoding grating that are placed at the ±1st diffraction orders of the decoding one [first term in Eq. (26)]. Because that digital postprocessing is produced with the addition of all the stored holograms, the frequency bands represented in the second term of Eq. (26) are also subtracted from the final Fourier distribution. Thus, only the second term in Eq. (26) contributes to distort the final result. But such contribution is not critical because it has much less intensity than the final superresolved image. Because the zeroth order of the object's spectrum is added 180 times in the central region (zeroth order of both encoding and decoding gratings), the contribution of the lateral frequency bands' addition in comparison with that of the reinforced zeroth order band will be negligible.

8. CONCLUSIONS

In this paper we have presented a wide review of superresolution techniques with special emphasis on techniques that imply time multiplexing while generating a synthetic aperture without changing optical parameters of the imaging systems. Moreover, a new superresolution approach based on rotating grating movement for temporally restricted objects in digital imaging systems has been described. This new approach is based on structured illumination incoming from a 1-D physical grating that is placed near but not in close contact with the input object. Thus, after performing the rotating grating approach and a digital postprocessing of the recorded sequence of images, a superresolved image is obtained in terms of a synthetic aperture generation. The presented approach has been mathematically analyzed and tested via computational simulations for two cases: digital imaging approach (DIA) and digital holographic imaging approach (DHIA). Both of these approaches can be directly applied to microscopy while yielding a superresolved synthetic aperture. As a result of the simulations presented, a 2-D resolution gain factor of 3 is achieved in comparison with the resolution of the same imaging system without using our approach. But a higher gain in resolving power can be achieved if the number of diffraction orders of the encoding grating is increased and the digital postprocessing is modified accordingly.

APPENDIX A: DESIRED RESULT

Bearing in mind that the SR principle presented here is based on the generation of a SA by addition of contiguous frequency bands of the object's spectrum, and in order to gain simplicity in the mathematical analysis, let us divide the FT of the object amplitude distribution in a set of contiguous circular apertures that generate the full object's spectrum as is depicted in Fig. 13. Mathematically, this assumption means that

$$\tilde{t}_F(u,v) = \sum_{\theta} \sum_{n} A_n \tilde{t}(u,v) \left[\mathrm{circ}\left(\frac{\rho}{\Delta \nu} \right) \otimes \delta(u + n\nu_0 \cos\theta, v + n\nu_0 \sin\theta) \right]. \tag{A1}$$

Equation (A1) represents the FT of the object after being filtered by a compound aperture equal to

$$H_n(u,v) = \sum_{\theta} \sum_{n} A_n \, \mathrm{circ}\left(\frac{\rho}{\Delta \nu} \right) \otimes \delta(u + n\nu_0 \cos\theta, v + n\nu_0 \sin\theta) \tag{A2}$$

and represents the desired result for the coherent case, that is, for DHIA of an optical system with unit magnification.

In the incoherent case and because the CCD performs an intensity recording process, we are interested in evaluating the FT of the intensity distribution captured by a CCD that is the autocorrelation of Eq. (A1):

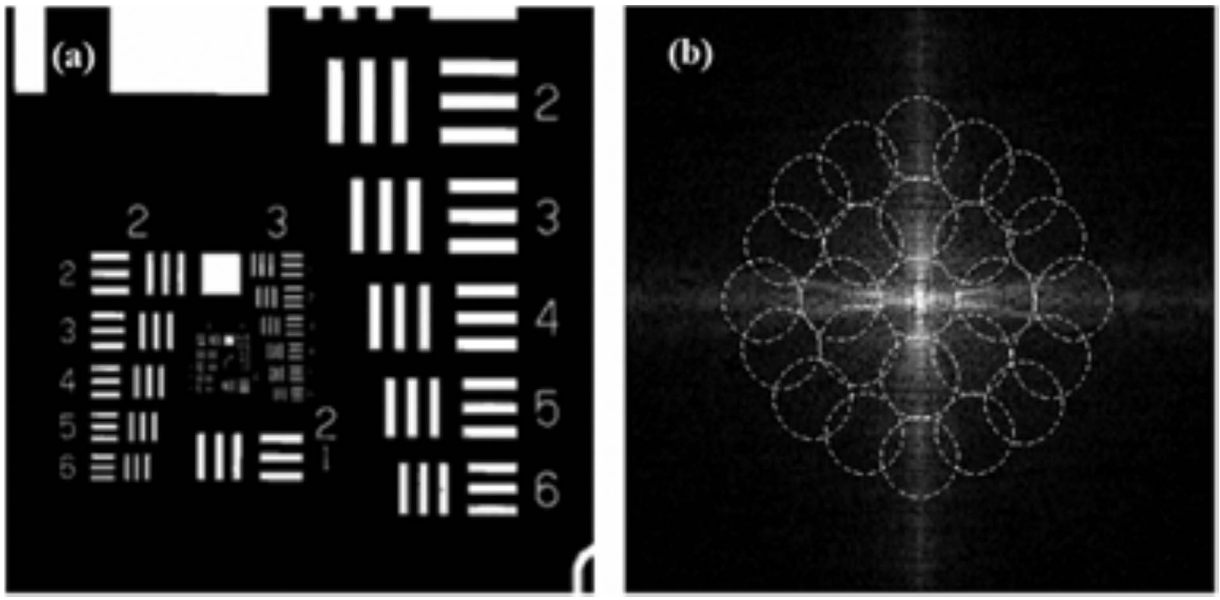


Fig. 13. (a) Object image and (b) its FT that can be separated in diffrerent contiguous circles.

$$FT[I_f(u,v)] = FT[|\tilde{t}_F(u,v)|^2] = \sum_{\theta} \sum_{n,m} A_n A_m{}^* [\tilde{t}(u,v) H_n(u,v)] * [\tilde{t}(u,v) H_m(u,v)], \quad \text{(A3)}$$

where $*$ denotes the autocorrelation. Thus, Eq. (A3) represents the output image that we want to receive from the SR system in the case of DIA.

ACKNOWLEDGMENT

This work was supported by FEDER funds and the Spanish Ministerio de Educacion y Ciencia under project FIS2007–60626.

REFERENCES

1. E. Abbe, "Beitrage zur theorie des mikroskops und der mikroskopischen wahrnehmung" Arch. Mikrosk. Anat. 9, 413–468 (1873).
2. J. W. Goodman, *Introduction to Fourier Optics* (McGraw-Hill, 1996).
3. D. Courjon, *Near-Field Microscopy and Near-Field Optics* (Imperial College Press, 2003).
4. Z. Zalevsky and D. Mendlovic, *Optical Super Resolution* (Springer, 2002).
5. M. Bertero, C. De Mol, "Super-resolution by data inversion," in E. Wolf. (ed.), *Progress in Optics, Vol. XXXVI* (Elsevier North-Holland, 1996), Chap. III, pp. 129–178.
6. P. Jacquinot, "Apodization," Prog. Opt. **3**, 29–186 (1964).
7. T. Wilson and C. J. Sheppard, *Theory and Practice of Scanning Optical Microscopy* (Academic, 1984).
8. G. Toraldo di Francia, "Resolving power and information," J. Opt. Soc. Am. **45**, 497–501 (1955).
9. G. Toraldo di Francia, "Degrees of freedom of an image," J. Opt. Soc. Am. **59**, 799–804 (1969).
10. I. J. Cox and J. R. Sheppard, "Information capacity and resolution in an optical system," J. Opt. Soc. Am. A **3**, 1152–1158 (1986).
11. A. J. den Dekker and A. van den Bos, "Resolution: a survey," J. Opt. Soc. Am. A **14**, 547–557 (1997).
12. W. Lukosz, "Optical systems with resolving powers exceeding the classical limits," J. Opt. Soc. Am. **56**, 1463–1472 (1966).
13. W. Lukosz, "Optical systems with resolving powers exceeding the classical limits II," J. Opt. Soc. Am. **57**, 932–941 (1967).
14. M. Francon, "Amélioration the résolution d'optique," Il Nuovo Cimento Suppl. **9**, 283–290 (1952).
15. A. Shemer, D. Mendlovic, Z. Zalevsky, J. García, and P. García-Martínez, "Superresolving optical system with time multiplexing and computer decoding," Appl. Opt. **38**, 7245–7251 (1999).
16. A. W. Lohmann and D. P. Paris, "Superresolution for nonbirefringent objects," Appl. Opt. **3**, 1037–1043 (1964).
17. A. I. Kartashev, "Optical system with enhanced resolving power," Opt. Spectra **9**, 204–206 (1960).
18. M. A. Grimm and A. W. Lohmann, "Superresolution image for one-dimensional object," J. Opt. Soc. Am. **56**, 1151–1156 (1966).
19. Z. Zalevsky, P. García-Martínez, and J. García, "Superresolution using gray level coding," Opt. Express **14**, 5178–5182 (2006).
20. D. Mendlovic and A. W. Lohman, "Space–bandwidth product adaptation and its application to super resolution: fundamentals," J. Opt. Soc. Am. A **14**, 558–562 (1997).
21. D. Mendlovic, A. W. Lohman, and Z. Zalevsky, "Space–bandwidth product adaptation and its application for super resolution: examples," J. Opt. Soc. Am. A **14**, 563–567 (1997).
22. E. Sabo, Z. Zalevsky, D. Mendlovic, N. Komforti, and I. Kiryushev, "Superresolution optical system with two fixed generalized Damman gratings," Appl. Opt. **39**, 5318–5325 (2000).
23. E. Sabo, Z. Zalevsky, D. Mendlovic, N. Komforti, and I. Kiryushev, "Superresolution optical system using three fixed generalized gratings: experimental results," J. Opt. Soc. Am. A **18**, 514–520 (2001).
24. A. Bachl and W. Lukosz, "Experiments on superresolution imaging of a reduced object field," J. Opt. Soc. Am. **57**, 163–169 (1967).
25. M. G. L. Gustafsson, "Surpassing the lateral resolution limit by a factor of two using structured illumination microscopy," J. Microsc. **198**, 82–87 (2000).
26. R. Heintzmann and P. A. Benedetti, "High-resolution image reconstruction in fluorescence microscopy with patterned excitation," Appl. Opt. **45**, 5037–5045 (2006).
27. J. Ryu, S. S. Hong, B. K. P. Horn, D. M. Freeman, and M. S. Mermelstein, "Multibeam interferometric illumination as the primary source of resolution in optical microscopy," Appl. Phys. Lett. **88**, 171112 (2006).
28. J. T. Frohn, H. F. Knapp, and A. Stemmer, "True optical resolution beyond the Rayleigh limit achieved by standing wave illumination," Proc. Natl. Acad. Sci. U.S.A. **97**, 7232–7236 (2000).
29. R. Heintzmann, T. M. Jovin, and C. Cremer, "Saturated patterned excitation microscopy—a concept for optical resolution improvement," J. Opt. Soc. Am. A **19**, 1599–1609 (2002).
30. M. G. L. Gustafsson, "Nonlinear structured illumination microscopy: wide-field fluorescence imaging with theoretically unlimited resolution," Proc. Natl. Acad. Sci. U.S.A. **102**, 13081–13086 (2005).
31. J. García, Z. Zalevsky, and D. Fixler, "Synthetic aperture superresolution by speckle pattern projection," Opt. Express **13**, 6073–6078 (2005).
32. E. Ben-Eliezer and E. Marom, "Aberration-free superresolution imaging via binary speckle pattern encoding and processing," J. Opt. Soc. Am. A **24**, 1003–1010 (2007).
33. B. J. Guo and S. L. Zhuang, "Image superresolution by using a source-encoding technique," Appl. Opt. **30**, 5159–5162 (1991).
34. Z. Zalevsky, J. García, P. García-Martínez, and C. Ferreira, "Spatial information transmission using orthogonal mutual coherence coding," Opt. Lett. **30**, 2837–2839 (2005).
35. E. N. Leith, D. Angell, and C.-P. Kuei, "Superresolution by incoherent-to-coherent conversion," J. Opt. Soc. Am. A **4**, 1050–1054 (1987).
36. V. Mico, Z. Zalevsky, P. García-Martínez, and J. García, "Single step superresolution by interferometric imaging," Opt. Express **12**, 2589–2596 (2004).
37. P. Massatsch, F. Charrière, E. Cuche, P. Marquet, and C. Depeursinge, "Time-domain optical coherence tomography with digital holographic microscopy," Appl. Opt. **44**, 1806–1812 (2005).
38. C. Iemmi, A. Moreno, and J. Campos, "Digital holography with a point-diffraction interferometer," Opt. Express **13**, 1885–1891 (2005).
39. X. Chen and S. R. J. Brueck, "Imaging interferometric lithography: approaching the resolution limits of optics," Opt. Lett. **24**, 124–126 (1999).
40. T. Colomb, P. Dahlgren, D. Beghuin, E. Cuche, P. Marquet, and C. Depeursinge, "Polarization imaging by use of digital holography," Appl. Opt. **41**, 27–37 (2002).
41. H. Medecki, E. Tejnil, K. A. Goldberg, and J. Bokor, "Phase-shifting point diffraction interferometer," Opt. Lett. **21**, 1526–1528 (1996).
42. T. Colomb, J. Kühn, F. Charrière, N. Aspert, P. Marquet, and C. Depeursinge, "Total aberration compensation in digital holographic microscopy with a reference conjugated hologram," Opt. Express **14**, 4300–4306 (2006).
43. I. Tamaguchi and T. Zhong, "Phase-shifting digital holography," Opt. Lett. **22**, 1268–1270 (1997).
44. C. J. Schwarz, Y. Kuznetsova, and S. R. J. Brueck, "Imaging interferometric microscopy," Opt. Lett. **28**, 1424–1426 (2003).
45. V. Mico, Z. Zalevsky, P. García-Martínez, and J. García,

"Superresolved imaging in digital holography by superposition of tilted wavefronts," Appl. Opt. **45**, 822–828 (2006).
46. V. Mico, Z. Zalevsky, and J. García, "Superresolution optical system by common-path interferometry," Opt. Express **14**, 5168–5177 (2006).
47. V. Mico, Z. Zalevsky, P. García-Martínez, and J. García, "Synthetic aperture superresolution using multiple off-axis holograms," J. Opt. Soc. Am. A **23**, 3162–3170 (2006).
48. S. A. Alexandrov, T. R. Hillman, T. Gutzler, and D. D. Sampson, "Synthetic aperture Fourier holographic optical microscopy," Phys. Rev. Lett. **97**, 168102 (2007).
49. J. R. Price, P. R. Bingham, and C. E. Thomas, Jr., "Improving resolution in microscopic holography by computationally fusing multiple, obliquely illuminated object waves in the Fourier domain," Appl. Opt. **46**, 826–833 (2007).
50. V. Mico, Z. Zalevsky, and J. García, "Synthetic aperture microscopy using off-axis illumination and polarization coding," Opt. Commun. **276**, 209–217 (2007).
51. J. García, D. Mas, and R. G. Dorsch, "Fractional-Fourier-transform calculation through the fast-Fourier-transform algorithm," Appl. Opt. **35**, 7013–7018 (1996).